



Nonlinear elastic vector solitons in hard-magnetic soft mechanical metamaterials

Quan Zhang^{a,*}, Andrei V. Cherkasov^a, Chen Xie^a, Nitesh Arora^b, Stephan Rudykh^{a,b}

^a School of Mathematical and Statistical Sciences, University of Galway, Galway H91 TK33, Ireland

^b Department of Mechanical Engineering, University of Wisconsin – Madison, Madison, WI 53706, United States

ARTICLE INFO

Keywords:

Hard-magnetic
Soft metamaterials
Magnetoactive elastomers
Finite deformations
Microstructure transformations
Solitary waves

ABSTRACT

We propose a design of a metamaterial for magnetically tunable propagation of nonlinear vector solitary waves. The metamaterial consists of a periodic array of units of hard-magnetic inclusion embedded in a soft matrix. The units are connected via thin and highly deformable ligaments. Our theoretical and numerical modeling results show that the configuration of the metamaterial undergoes drastic transformations when activated by a magnetic field. These controllable microstructural transformations significantly influence the propagation of vector solitary waves in the proposed metamaterial system. We report the *magnetic field-enabled* propagation of solitary waves. We show that the proposed soft magnetoactive metamaterial allows us to tune the key characteristics of the enabled nonlinear solitary waves, including their pulse width and amplitude. Our findings also highlight the potential of magneto-mechanical coupling in the development of untethered mechanical metamaterial systems for applications in nondestructive testing, energy harvesting, and smart soft wave devices.

1. Introduction

Originated in their highly ordered microstructures, mechanical metamaterials enable the control and manipulation of elastic waves in unprecedented ways: They facilitate applications ranging from vibration isolation (Bilal et al., 2017a; Hussein et al., 2014; Krushynska et al., 2023; Wang et al., 2014; Zhang et al., 2021), waveguiding (Bilal et al., 2017b; Chen et al., 2020; Liu et al., 2019; Wang et al., 2016), negative refraction (Liu et al., 2011; Mokhtari et al., 2019; Srivastava, 2016; Zhu et al., 2014), focusing (Memoli et al., 2017), and invisible cloaking (Nassar et al., 2019, 2020; Zhang et al., 2020a) to manipulations of the topological state of matter (Chen et al., 2018; Chen et al., 2019; Chen et al., 2021b; Foehr et al., 2018; Wang et al., 2015; Zhang et al., 2019a, 2020b) that enables elastic wave flows immune to backscattering-induced losses. While small-amplitude motion phenomena have been explored, only limited knowledge exists in the important area of nonlinear wave behavior, even though they offer great promise for controlling mechanical signals (Chen et al., 2014; Coulais et al., 2017; Raney et al., 2016) and revealing such unique effects as one-way propagation (Nadkarni et al., 2016).

Here, we focus on an important class of nonlinear phenomena – solitary waves, which have been observed in various physical systems.

They were first reported by John Scott Russell (Russell, 1844) in nonlinear wave packets of water propagating with a stable shape and constant velocity in the Scottish Union Canal. The unique properties of solitary waves have been studied and exploited in many fields of science and engineering, including photonics (Christodoulides et al., 2003), optical communication (Marin-Palomo et al., 2017), frequency conversion (Hwang and Arrieta, 2021), structural morphing (Zareei et al., 2020; Zhang et al., 2019b), and nondestructive testing (Singhal et al., 2017). For mechanical systems, granular crystals have been found to provide a material platform supporting propagation of nonlinear solitary waves (Chong et al., 2017; Porter et al., 2015; Sen et al., 2008). However, the granular media only support *scalar* solitons that lack the typical multi-polarization of elastic waves propagating in classical solids. Moreover, nonlinear responses in these granular systems are determined by the contacts between particles – they are difficult to control even in relatively simple 2D settings (Deng et al., 2017), and pose significant challenges in fully 3D settings.

Soft materials provide attractive media for realizing nonlinear elastic wave phenomena. Thus, various types of solitons have been demonstrated in microstructured soft metamaterial designs (Deng et al., 2021). Above all, since soft metamaterials can usually support tensile deformation, the propagation of *rarefaction* solitons has been reported (Deng

* Corresponding author.

E-mail address: quan.zhang@universityofgalway.ie (Q. Zhang).

et al., 2020; Yasuda et al., 2019). Note that the granular systems may not support rarefaction solitons due to their lack of tensile cohesion. Moreover, soft mechanical metamaterials, with pre-designed bistable or multi-stable system behavior, can support the propagation of *topological* solitons or transition waves. In such systems, the nonlinear pulse propagates as the structural union phase transformation front (Jin et al., 2020; Nadkarni et al., 2016; Raney et al., 2016; Yasuda et al., 2020). Furthermore, it has been shown that soft mechanical metamaterials comprising arrays of rigid units that are connected by thin and highly deformable ligaments support the propagation of elastic *vector* solitons. Such vector solitary pulse consists of both translational and rotational components – they are coupled together and propagate together without distortion due to the perfect balance between system dispersion and nonlinearity (Deng et al., 2019a; Deng et al., 2017; Deng et al., 2018b). However, the characteristics of the solitary waves in these soft metamaterial systems can be tuned only through direct mechanical loading (Deng et al., 2018a; Deng et al., 2019b) owing to the *passive* nature of their constitutive materials.

Soft *active* materials can undergo reversible changes in their properties and transformations in shape induced by external stimuli, such as light (Palagi et al., 2016), heat (Zhang et al., 2015; Zhang et al., 2016), electric (Galich and Rudykh, 2017; Wu et al., 2017) or magnetic fields (da Costa et al., 2022; Erb et al., 2012; Goshkoderia et al., 2020; Pathak et al., 2022; Rudykh and Bertoldi, 2013). Magnetoactive elastomers (MAEs) – a class of soft active materials that respond to magnetic field excitation – are a promising material platform for untethered devices thanks to their simple, remote, and reversible principle of actuation. Typically, MAEs consist of magnetizable particles embedded into a soft matrix. The application of an external magnetic field produces complex interactions between the magnetized particles, resulting in the overall deformation of the material and the modification of its effective properties (Chen et al., 2023; Ciambella et al., 2018; Goshkoderia and Rudykh, 2017; Itskov and Khiêm, 2016; Keip and Rambaussek, 2016; Ortigosa and Gil, 2016). Potential applications include variable-stiffness devices (Erb et al., 2012), actuators (Moreno-Mateos et al., 2022; Tang et al., 2018) and sensors (Tian et al., 2011), soft robotics (Cui et al., 2019; Hu et al., 2018), metamaterials (Chen et al., 2021a; Yu et al., 2018), and biomedical devices (Wang et al., 2021).

The tunability of materials by a remote magnetic field – either through property modification or induced deformation – holds intriguing potential for designing metamaterials for manipulating elastic waves. The “small-on-large” framework has been employed to examine the propagation of small-amplitude elastic waves in finitely deformed magneto-elastic materials. The theoretical analysis of elastic waves in MAEs builds on the fundamental work (Destrade and Ogden, 2011; Maugin, 1981) establishing the governing equations for small-amplitude motions superimposed on the finitely deformed state. The framework has been employed for the analysis of small-amplitude elastic waves in periodic laminates (Karami Mohammadi et al., 2019). These studies have considered *soft*-magnetic active elastomers (typically consisting of iron, soft ferrite, iron–silicon alloys, or iron–nickel alloy particles embedded in a soft matrix) that are not activated without an externally applied magnetic field. In contrast, *hard*-magnetic active elastomers (hMAEs) retain their magnetization even after the external field has been removed. Their high coercivity allows the hard-magnetic materials to sustain their remanent magnetization over a wide range of applied magnetic fields (that are below the coercive field strength) (Garcia-Gonzalez et al., 2023; Kim et al., 2018; Lucarini et al., 2022; Yan et al., 2021; Zhao et al., 2019). Recently, Zhang and Rudykh (2022) examined the propagation of small-amplitude shear waves in hMAE periodic laminates. Zhang et al. (2023) proposed an hMAE-based asymmetric mechanical metamaterial design that allows remote and reversible control of the metamaterial performance. These results predict the existence of band gaps (a typical phenomenon for small-amplitude linear elastic waves) that can be tuned by an external magnetic field.

In this work, we investigate the conditions for the existence of

solitary waves enabled by a magnetic field in hard-magnetic soft mechanical metamaterial (hSMM) systems. We propose to exploit the unique magneto-mechanical coupling of hMAEs to *remotely* tune the width, amplitude, and velocity of the nonlinear solitary waves propagating within. The developed novel hSMM can be used as a solitary wave switch to provide on or off capabilities. The remainder of this paper is organized as follows: Section 2 presents the governing equations of the proposed hSMM system, by approximating it as an array of rigid bodies connected at the vertices via a combination of longitudinal, shearing, and rotational springs. Section 3 focuses on the magnetic field-induced deformation in the quasi-static regime. We theoretically and numerically investigate the deformation induced in the proposed hSMMs as a function of the externally applied magnetic field. In Section 4, we identify the planar nonlinear solitary waves supported by the magnetoactive system and investigate their dependence on externally applied magnetic stimuli. Section 5 provides a summary and concluding remarks.

2. Hard-magnetic soft mechanical metamaterials

2.1. Geometry and constitutive components

Fig. 1 illustrates the design of the proposed hSMM. The system consists of an array of identical squares connected at their vertices via thin and highly deformable ligaments (Fig. 1a). All squares have a center-to-center distance of a , and neighboring squares are alternately rotated by an offset angle of θ_0 (between the diagonal of the square and the vertical direction) in the clockwise and counterclockwise directions; the width of the thin ligaments is denoted by t (Fig. 1b). Each square unit is embedded with an hMAE core (with radius r) that can be fabricated by casting and curing the mixture of hard-magnetic particles and the elastomer resin in molds (Fig. 1a). Throughout this study, we consider the hSMM composites with $r = a/(3\sqrt{2}\cos\theta_0)$. The hMAE core is characterized by the remanent magnetization \mathbf{M}_0 in the reference configuration. The application of an external magnetic field \mathbf{B} induces the magnetic body torque, $\tau_{\text{magnetic}} = \mathbf{M} \times \mathbf{B}$, where $\mathbf{M} = \mathbf{R}\mathbf{M}_0$ is the magnetization in the current configuration and \mathbf{R} denotes the rotation tensor. The magnetically induced torque acts to align the direction of magnetization of the core with the applied magnetic field (Fig. 1b). As a result, the hMAE core rotates, leading to the overall shrinkage or expansion of the lattice system.

The initial shear modulus and density of the soft matrix are $G_0 = 200$ kPa and $\rho_0 = 1160$ kg/m³ (corresponding to the commercial polydimethylsiloxane (PDMS) used in Wang et al. (2021)), respectively. The hMAE core is modeled as a PDMS doped by neodymium–iron–boron (NdFeB, with remanent magnetization magnitude $M_N = 640$ kA/m and density $\rho_N = 7610$ kg/m³, see Wang et al. (2021)) particles. The volume fraction of the NdFeB particles in the hMAE core is denoted by ϕ . The remanent magnetization of the core is estimated as $M = M_N\phi$. Based on the Mooney model (Mooney, 1951), the shear modulus of the hMAE core is estimated as $G(\phi) = G_0\exp[2.5\phi/(1 - 1.35\phi)]$. Here, the volume fraction of NdFeB particles in the hMAE core is taken to be $\phi = 0.1$; thus, the core is modeled with a shear modulus $G = 267$ kPa, density $\rho = 1805$ kg/m³, and remanent magnetization $M = 64$ kA/m.

2.2. Discrete model

The above auxetic system made of rotating squares can be approximated as an array of rigid bodies connected at the vertices via a combination of longitudinal, shearing, and rotational springs. This approach has been shown to be accurate in a similar purely mechanical metamaterial system (Deng et al., 2019a; Deng et al., 2017). Note that we introduce magneto-mechanical coupling, and derive the corresponding analytical solutions for the magnetic field-induced deformation and superimposed nonlinear motion.

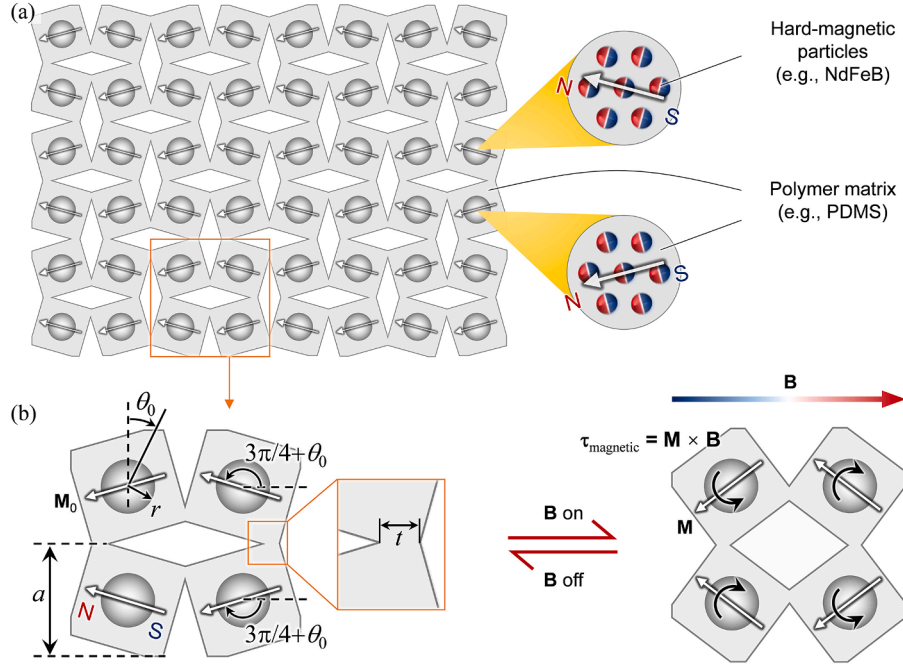


Fig. 1. Schematics of the hSMM. (a) The reference configuration comprises an array of square units connected by thin and highly deformable ligaments; there is an hMAE core inside each square unit. (b) The definitions of the geometric parameters (including the initial offset angle θ_0 of the squares, the center-to-center distance a , the radius r of the hMAE cores, and the thickness t of the ligaments). The configuration of the proposed metamaterial system can be tuned by external magnetic fields.

We assume that the square units are rigid and have three degrees of freedom: displacement in the x -direction, u_x , displacement in the y -direction, u_y , and rotation around the z -direction, θ . The positive direction of rotation is defined alternately for neighboring squares; the positive direction of rotation for each unit is assumed to be the energetically favorable direction of rotation under compression. Specifically, for the $[i, j]$ -th unit (which has an offset angle of θ_0 in the clockwise direction; see Fig. 2a), a clockwise rotation is positive (denoted by the orange arrow in Fig. 2a), while for the $[i-1, j]$ -th, $[i+1, j]$ -th, $[i, j-1]$ -th, and $[i, j+1]$ -th units (which have an offset angle of θ_0 in the counterclockwise direction; see Fig. 2a), a counterclockwise rotation is positive (denoted by the green arrow in Fig. 2a).

The ligaments connecting neighboring units are modeled as a combination of three linear springs: i) a spring with stiffness k_l that captures the longitudinal response, ii) a spring with stiffness k_s that captures the shear response, and iii) a spring with stiffness k_θ that captures the rotational response. The values of k_l , k_s , and k_θ are determined via finite

element simulations of the responses of two squares connected by a single ligament (see Appendix A for details).

2.3. Governing equations

We first express the deformation of the springs by using the degrees of freedom of the square units. Consider the $[i, j]$ -th unit as shown in Fig. 2b; let $\Delta\theta_h^{[i,j]}$ and $\Delta\theta_v^{[i,j]}$ denote the changes in angle experienced by the rotational spring connecting the $[i, j]$ -th and $[i, j+1]$ -th units and the rotational spring connecting the $[i, j]$ -th and $[i+1, j]$ -th units, respectively. We then have,

$$\Delta\theta_h^{[i,j]} = \theta^{[i,j]} + \theta^{[i,j+1]}, \Delta\theta_v^{[i,j]} = \theta^{[i,j]} + \theta^{[i+1,j]}. \quad (1)$$

Moreover, the vector $\mathbf{r}_p^{[i,j]}$ that connects the center of the $[i, j]$ -th unit to its p -th ($p = 1, 2, 3, 4$) vertex can be written as,

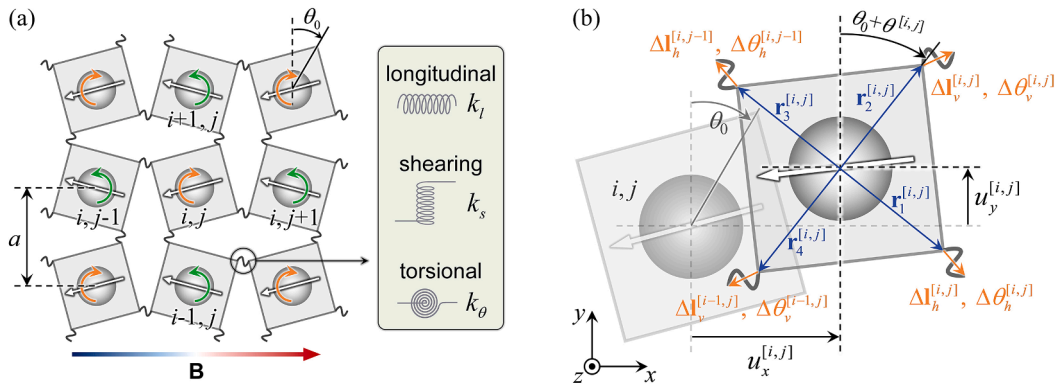


Fig. 2. (a) The discrete model comprising rigid square units connected at their vertices by springs. (b) The $[i, j]$ -th square unit before and after deformation.

$$\begin{aligned}
\mathbf{r}_1^{[i,j]}(\theta^{[i,j]}) &= \frac{a}{2\cos(\theta_0)} [\cos(\theta_0 + \theta^{[i,j]}), -(-1)^{i+j}\sin(\theta_0 + \theta^{[i,j]})], \\
\mathbf{r}_2^{[i,j]}(\theta^{[i,j]}) &= \frac{a}{2\cos(\theta_0)} [(-1)^{i+j}\sin(\theta_0 + \theta^{[i,j]}), \cos(\theta_0 + \theta^{[i,j]})], \\
\mathbf{r}_3^{[i,j]}(\theta^{[i,j]}) &= \frac{a}{2\cos(\theta_0)} [-\cos(\theta_0 + \theta^{[i,j]}), (-1)^{i+j}\sin(\theta_0 + \theta^{[i,j]})], \\
\mathbf{r}_4^{[i,j]}(\theta^{[i,j]}) &= \frac{a}{2\cos(\theta_0)} [(-1)^{i+j}\sin(\theta_0 + \theta^{[i,j]}), \cos(\theta_0 + \theta^{[i,j]})].
\end{aligned} \quad (2)$$

Let us define vector $\Delta \mathbf{l}_h^{[i,j]}$ with entries corresponding to the changes in length along the x - and y -directions of the linear spring connecting the $[i, j]$ -th and $[i, j + 1]$ -th units; and vector $\Delta \mathbf{l}_v^{[i,j]}$ contains entries corresponding to the changes in length along the x - and y -directions of the linear spring connecting the $[i, j]$ -th and $[i + 1, j]$ -th units. Thus, we obtain

$$\begin{aligned}
\Delta \mathbf{l}_h^{[i,j]} &= (u_x^{[i,j+1]} - u_x^{[i,j]})\mathbf{e}_x + (u_y^{[i,j+1]} - u_y^{[i,j]})\mathbf{e}_y + \Delta \mathbf{r}_3^{[i,j+1]} - \Delta \mathbf{r}_1^{[i,j]}, \\
\Delta \mathbf{l}_v^{[i,j]} &= (u_x^{[i+1,j]} - u_x^{[i,j]})\mathbf{e}_x + (u_y^{[i+1,j]} - u_y^{[i,j]})\mathbf{e}_y + \Delta \mathbf{r}_4^{[i+1,j]} - \Delta \mathbf{r}_2^{[i,j]},
\end{aligned} \quad (3)$$

where

$$\Delta \mathbf{r}_p^{[i,j]} = \mathbf{r}_p^{[i,j]}(\theta^{[i,j]}) - \mathbf{r}_p^{[i,j]}(0). \quad (4)$$

Therefore, the elastic potential energy in the $[i, j]$ -th horizontal ligament that connects the $[i, j]$ -th and $[i, j + 1]$ -th units can be written as

$$U_{e-h}^{[i,j]} = \frac{1}{2} \left[k_t (\Delta \mathbf{l}_h^{[i,j]} \cdot \mathbf{e}_x)^2 + k_s (\Delta \mathbf{l}_h^{[i,j]} \cdot \mathbf{e}_y)^2 + k_\theta (\Delta \theta_h^{[i,j]})^2 \right], \quad (5)$$

and the elastic potential energy in the $[i, j]$ -th vertical ligament that connects the $[i, j]$ -th and $[i + 1, j]$ -th units can be written as

$$U_{e-v}^{[i,j]} = \frac{1}{2} \left[k_t (\Delta \mathbf{l}_v^{[i,j]} \cdot \mathbf{e}_y)^2 + k_s (\Delta \mathbf{l}_v^{[i,j]} \cdot \mathbf{e}_x)^2 + k_\theta (\Delta \theta_v^{[i,j]})^2 \right]. \quad (6)$$

Next, we introduce the estimates for the magnetic interaction between neighboring hMAE cores (Liang et al., 2022; Slesarenko, 2020). The magnetic potential energy between the $[i, j]$ -th and $[i, j + 1]$ -th units, denoted by $U_{m-h}^{[i,j]}$, and the magnetic potential energy between the $[i, j]$ -th and $[i + 1, j]$ -th units, denoted by $U_{m-v}^{[i,j]}$, are

$$\begin{aligned}
U_{m-h}^{[i,j]} &= -\frac{\mu_0}{4\pi |\mathbf{a}_h^{[i,j]}|^3} \left[3(V_m \mathbf{M}^{[i,j]} \cdot \hat{\mathbf{a}}_h^{[i,j]})(V_m \mathbf{M}^{[i,j+1]} \cdot \hat{\mathbf{a}}_h^{[i,j]}) - V_m \mathbf{M}^{[i,j]} \cdot V_m \mathbf{M}^{[i,j+1]} \right], \\
U_{m-v}^{[i,j]} &= -\frac{\mu_0}{4\pi |\mathbf{a}_v^{[i,j]}|^3} \left[3(V_m \mathbf{M}^{[i,j]} \cdot \hat{\mathbf{a}}_v^{[i,j]})(V_m \mathbf{M}^{[i+1,j]} \cdot \hat{\mathbf{a}}_v^{[i,j]}) - V_m \mathbf{M}^{[i,j]} \cdot V_m \mathbf{M}^{[i+1,j]} \right],
\end{aligned} \quad (7)$$

where μ_0 is the magnetic permeability of the vacuum, V_m is volume of the hMAE core, and $\mathbf{M}^{[i,j]}$ is the remanent magnetization of the $[i, j]$ -th hMAE core in the deformed configuration,

$$\mathbf{M}^{[i,j]} = M \cos(\theta_m^{[i,j]})\mathbf{e}_x + M \sin(\theta_m^{[i,j]})\mathbf{e}_y, \quad (8)$$

where M is the value of the remanent magnetization of the hMAE core as given in Sec. 2.1, and

$$\theta_m^{[i,j]} = -(-1)^{i+j} \left(\frac{3}{4} \pi + \theta_0 + \theta^{[i,j]} \right). \quad (9)$$

In addition, $\mathbf{a}_h^{[i,j]}$ is the separation vector between the centers of the $[i, j]$ -th and the $[i, j + 1]$ -th hMAE cores, and $\mathbf{a}_v^{[i,j]}$ is the separation vector between the centers of the $[i, j]$ -th and the $[i + 1, j]$ -th hMAE cores,

$$\begin{aligned}
\mathbf{a}_h^{[i,j]} &= (a + u_x^{[i,j+1]} - u_x^{[i,j]})\mathbf{e}_x + (u_y^{[i,j+1]} - u_y^{[i,j]})\mathbf{e}_y, \\
\mathbf{a}_v^{[i,j]} &= (u_x^{[i+1,j]} - u_x^{[i,j]})\mathbf{e}_x + (a + u_y^{[i+1,j]} - u_y^{[i,j]})\mathbf{e}_y,
\end{aligned} \quad (10)$$

and their unit vectors are $\hat{\mathbf{a}}_h^{[i,j]} = \mathbf{a}_h^{[i,j]} / |\mathbf{a}_h^{[i,j]}|$ and $\hat{\mathbf{a}}_v^{[i,j]} = \mathbf{a}_v^{[i,j]} / |\mathbf{a}_v^{[i,j]}|$,

respectively.

Lastly, the magnetic potential energy that accounts for the interaction between the $[i, j]$ -th hMAE core and the externally applied magnetic field \mathbf{B} is

$$U_{m-d}^{[i,j]} = -V_m \mathbf{M}^{[i,j]} \cdot \mathbf{B}. \quad (11)$$

In this study, the magnetic field is considered to be in the horizontal direction (see Fig. 2), namely, $\mathbf{B} = B\mathbf{e}_x$.

The kinematic energy of the $[i, j]$ -th unit is,

$$V^{[i,j]} = \frac{1}{2} \left[M_g \left(\dot{u}_x^{[i,j]} \right)^2 + M_g \left(\dot{u}_y^{[i,j]} \right)^2 + J \left(\dot{\theta}^{[i,j]} \right)^2 \right], \quad (12)$$

where M_g and J are the mass and moment of inertia of these identical square units, respectively. Consider a lattice system comprising N_x square units along the x -direction and N_y square units along the y -direction. The Lagrangian is,

$$\begin{aligned}
L &= \sum_{i=1}^{N_y} \sum_{j=1}^{N_x} V^{[i,j]} - \sum_{i=1}^{N_y} \sum_{j=1}^{N_x-1} U_{e-h}^{[i,j]} - \sum_{j=1}^{N_x} \sum_{i=1}^{N_y-1} U_{e-v}^{[i,j]} - \sum_{i=1}^{N_y} \sum_{j=1}^{N_x-1} U_{m-h}^{[i,j]} - \sum_{j=1}^{N_x} \sum_{i=1}^{N_y-1} U_{m-v}^{[i,j]} \\
&\quad - \sum_{i=1}^{N_y} \sum_{j=1}^{N_x} U_{m-d}^{[i,j]}.
\end{aligned} \quad (13)$$

By using Lagrange's principle, the equations of motion of the $[i, j]$ -th unit can be obtained as,

$$\frac{d}{dt} \left(\frac{\partial L}{\partial \dot{u}_x^{[i,j]}} \right) - \frac{\partial L}{\partial u_x^{[i,j]}} = 0, \frac{d}{dt} \left(\frac{\partial L}{\partial \dot{u}_y^{[i,j]}} \right) - \frac{\partial L}{\partial u_y^{[i,j]}} = 0, \frac{d}{dt} \left(\frac{\partial L}{\partial \dot{\theta}^{[i,j]}} \right) - \frac{\partial L}{\partial \theta^{[i,j]}} = 0. \quad (14)$$

The specific formulae of the equations of motion are presented in Appendix B (Eqs. (42)–(44)) and are not repeated here.

3. Magneto-mechanical behavior in the quasi-static regime

3.1. Magnetically-induced global deformation

Here, we use the proposed model to estimate the magnetically-induced deformation of the hSMM in the quasi-static regime. We consider the hSMM system subjected to an external magnetic field in the horizontal direction (coinciding with one of the principal directions of the material). For such an actuating condition,

(i) the inertial terms vanish,

$$\frac{\partial^2 u_x^{[i,j]}}{\partial t^2} = \frac{\partial^2 u_y^{[i,j]}}{\partial t^2} = \frac{\partial^2 \theta^{[i,j]}}{\partial t^2} = 0, \forall i, j; \quad (15)$$

(ii) consider hSMM lattice systems with even rows and even columns of unit cells, the total magnetic torque experienced by the hSMM system is zero, and the deformation is homogeneous,

$$\begin{aligned}
u_x^{[i+1,j]} &= u_x^{[i,j]}, u_y^{[i,j+1]} = u_y^{[i,j]}, \\
u_x^{[i,j+1]} - u_x^{[i,j]} &= a\epsilon_{st}^x, u_y^{[i+1,j]} - u_y^{[i,j]} = a\epsilon_{st}^y, \\
\theta^{[i,j]} &= \theta_{st}, \forall i, j,
\end{aligned} \quad (16)$$

where ϵ_{st}^x and ϵ_{st}^y are the macroscopic strains in the x - and y -directions, respectively, and θ_{st} is the absolute value of rotation angle of the square units (recall that the neighboring units rotate in opposite directions) due to the activation by the external magnetic field; and

- (iii) the mechanical and magnetic forces in the x-direction (between the $[i, j]$ -th and $[i, j + 1]$ -th units), and in the y-direction (between the $[i, j]$ -th and $[i + 1, j]$ -th units) are balanced due to the mechanical traction-free boundary conditions, namely,

$$\frac{\partial U_{e-h}^{[i,j]}}{\partial u_x^{[i,j]}} + \frac{\partial U_{m-h}^{[i,j]}}{\partial u_x^{[i,j]}} = 0, \quad \frac{\partial U_{e-v}^{[i,j]}}{\partial u_y^{[i,j]}} + \frac{\partial U_{m-v}^{[i,j]}}{\partial u_y^{[i,j]}} = 0. \quad (17)$$

By substituting Eqs. (15) and (16) into Eq. (14), and Eq. (16) into Eq. (17), we obtain

$$\begin{aligned} & -8k_0\theta_{st} - \frac{k_l a^2}{\cos\theta_0} \sin(\theta_{st} + \theta_0) (2 + \varepsilon_{st}^x + \varepsilon_{st}^y) + \frac{2k_l a^2}{\cos^2\theta_0} \sin(\theta_{st} + \theta_0) \cos(\theta_{st} + \theta_0) \\ & + \frac{\mu_0 M^2 V_m^2}{4\pi a^3 (1 + \varepsilon_{st}^x)^3} \cos(2\theta_{st} + 2\theta_0) + \frac{\mu_0 M^2 V_m^2}{4\pi a^3 (1 + \varepsilon_{st}^y)^3} \cos(2\theta_{st} + 2\theta_0) \\ & - MBV_m \cos\left(\frac{\pi}{4} + \theta_{st} + \theta_0\right) = 0, \\ & k_l a \left[1 + \varepsilon_{st}^x - \frac{\cos(\theta_{st} + \theta_0)}{\cos(\theta_0)} \right] + \frac{3\mu_0 M^2 V_m^2}{8\pi a^4 (1 + \varepsilon_{st}^x)^4} [3 + \sin(2\theta_{st} + 2\theta_0)] = 0, \\ & k_l a \left[1 + \varepsilon_{st}^y - \frac{\cos(\theta_{st} + \theta_0)}{\cos(\theta_0)} \right] + \frac{3\mu_0 M^2 V_m^2}{8\pi a^4 (1 + \varepsilon_{st}^y)^4} [-3 + \sin(2\theta_{st} + 2\theta_0)] = 0. \end{aligned} \quad (18)$$

By solving Eq. (18) we can determine the strains ε_{st}^x and ε_{st}^y (along the two principal directions) as well as the rotation of the square units θ_{st} for a given magnetic field B .

3.2. Finite element simulation results and comparison with the analytical estimates

We construct a finite-sized numerical model (e.g., consisting of 10×10 square units) in 2D under the plane-strain conditions. The equations of equilibrium and the magneto-static equations are solved in COMSOL Multiphysics 6.0. Magneto-mechanical coupling is established by introducing the total stress depending on the magnetic field (Zhang and Rudykh, 2022), namely,

$$\sigma_{total} = \sigma_{el} + \frac{1}{\mu} \mathbf{B} \otimes \mathbf{B} - \frac{1}{\mu_r} \mathbf{M} \otimes \mathbf{B}, \quad (19)$$

where σ_{el} denotes the purely elastic component of stress, μ is the permeability of the material, and $\mu_r = \mu/\mu_0$ is its relative magnetic permeability. The external magnetic field is applied in the horizontal direction, and the distribution of remanent magnetizations is illustrated in Fig. 1. The mechanical response of the constitutive materials is described by the neo-Hookean model.

Fig. 3 displays the magnetic field-induced deformation in the hSMMs with a center-to-center distance $a = 10$ mm, initial offset angle $\theta_0 = 5^\circ$, and ligament thickness $t = 0.04a$. Fig. 3a shows the dependence of the macroscopic strains ε_{st}^x and ε_{st}^y on the magnetic field intensity B . The curves correspond to the analytical estimates through Eq. (18), with $k_l = 559.2$ N/m, $k_s = 144.0$ N/m, and $k_\theta = 36.1 \times 10^{-6}$ N·m (the values are determined numerically – see the details in Appendix A – for the lattice with the out-of-plane thickness $h = 0.3a$). The discrete points are the results of the finite element simulations. We note that the analytical estimates agree with the finite element simulation results. In the finite element simulations, the macroscopic strains are obtained by measuring the difference in displacement between target points, as marked in Fig. 3c(ii); these two points are antisymmetric about the center $(0, 0)$ of the finite-sized lattice, and the strains are measured as,

$$\varepsilon_{st}^x = \frac{u_{\text{point 1}} - u_{\text{point 2}}}{3a}, \quad \varepsilon_{st}^y = \frac{v_{\text{point 1}} - v_{\text{point 2}}}{3a}, \quad (20)$$

where $u_{\text{point 1}}$ and $u_{\text{point 2}}$ ($v_{\text{point 1}}$ and $v_{\text{point 2}}$) are displacements of points 1 and 2 along the x-direction (y-direction), respectively. Fig. 3b illustrates the rotation of the square units θ_{st} as a function of the magnetic field B . Good agreement is observed between the theoretical and finite element simulation results. The rotation direction of the square units is reversed as the direction of the applied magnetic field changes, as shown by the deformed configurations for $B = -30$ mT (Fig. 3c(i)) and $B = 30$ mT (Fig. 3c(iii)). Moreover, the stress is mainly localized at the thin ligaments of the deformed lattice activated by the external magnetic field (Fig. 3c). This observation is in line with the assumption introduced for deriving the discrete mass-spring model-based estimates.

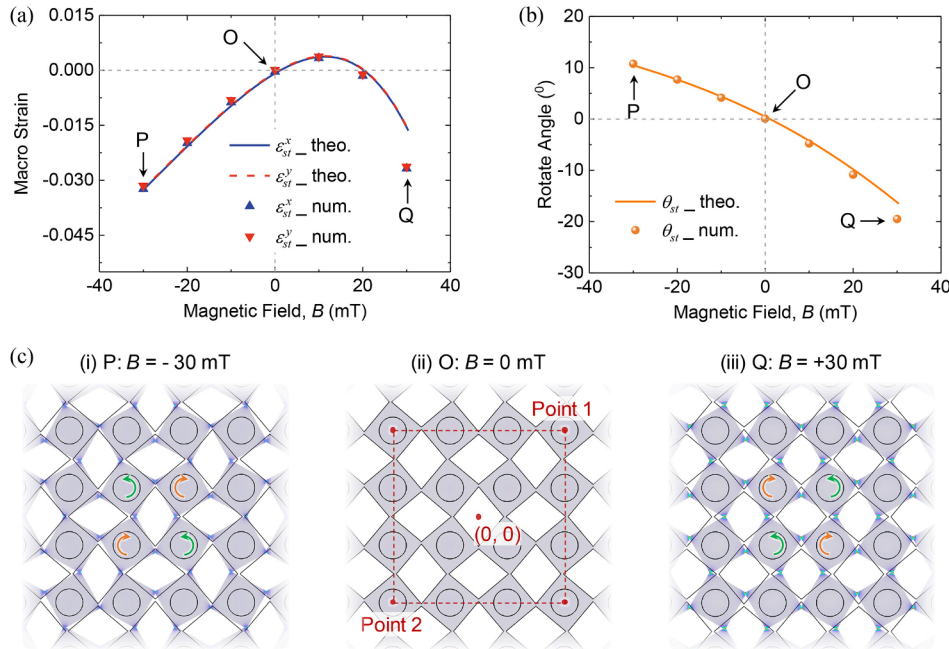


Fig. 3. Magnetic field-induced deformation in the hSMM system with geometric parameters $a = 10$ mm, $\theta_0 = 5^\circ$, and $t = 0.04a$. (a) The macroscopic strains ε_{st}^x and ε_{st}^y as a function of the magnetic field B . (b) The rotation of the square units θ_{st} as a function of the magnetic field B . (c) The deformed configurations corresponding to positions P, O, and Q (as marked in a and b).

Fig. 4 shows variations in the magneto-mechanical deformation versus the applied magnetic field for the hSMMs with various geometric parameters. The results are shown for the hSMMs with a fixed center-to-center distance of $a = 10$ mm. For all the considered cases, the analytically estimated deformations agree well with the finite element simulation results. An increment in the ligament thickness t increases its stiffness, thus, significantly changing the magnetic field level required to actuate the hSMM. For instance, the magnetic field level required to rotate the square units by -12° for a hSMM with $\theta_0 = 10^\circ$ and $t = 0.04a$ is $B = 24.8$ mT (see Fig. 4a); in contrast, that for a hSMM with $\theta_0 = 10^\circ$ and $t = 0.06a$ is increased to $B = 53.6$ mT (see Fig. 4b). In addition, as the initial offset angle θ_0 increases, a larger magnetic field-induced expansion (with positive macro strains) is observed under the actuating field applied in the $+x$ direction. For example, the maximum positive strain value in the hSMM with $\theta_0 = 5^\circ$ and $t = 0.06a$ is $+0.0038$ (see Fig. 4c), while that in the hSMM with $\theta_0 = 10^\circ$ and $t = 0.06a$ is $+0.0154$ (see Fig. 4b).

4. Propagation of planar nonlinear solitary waves

4.1. Equations of motion for the superimposed nonlinear waves

In this section, we consider the planar nonlinear motion superimposed on the hSMM deformed by external magnetic fields. The total displacements and rotation of the $[i, j]$ -th square unit can be written as,

$$u_x^{[ij]} = u_{x-st}^{[ij]} + u_{x-w}^{[ij]}, u_y^{[ij]} = u_{y-st}^{[ij]} + u_{y-w}^{[ij]}, \theta^{[ij]} = \theta_{st}^{[ij]} + \theta_w^{[ij]}, \quad (21)$$

where $u_{x-st}^{[ij]}$, $u_{y-st}^{[ij]}$, and $\theta_{st}^{[ij]}$ are the displacements and rotation induced by the magneto-mechanical pre-deformation, and satisfy Eqs. (15) and (16), and $u_{x-w}^{[ij]}$, $u_{y-w}^{[ij]}$, and $\theta_w^{[ij]}$ are the displacements and rotation generated by the propagating nonlinear wave. Upon substitution of Eq. (21) into Eq. (13), the equations of motion for the superimposed wave can be obtained as,

$$\frac{d}{dt} \left(\frac{\partial L}{\partial \dot{u}_{x-w}^{[ij]}} \right) - \frac{\partial L}{\partial u_{x-w}^{[ij]}} = 0, \frac{d}{dt} \left(\frac{\partial L}{\partial \dot{u}_{y-w}^{[ij]}} \right) - \frac{\partial L}{\partial u_{y-w}^{[ij]}} = 0, \frac{d}{dt} \left(\frac{\partial L}{\partial \dot{\theta}_w^{[ij]}} \right) - \frac{\partial L}{\partial \theta_w^{[ij]}} = 0. \quad (22)$$

The specific formulae of Eq. (22) are given in Appendix C (Eqs. (45)–(47)), which can be solved only numerically.

4.2. Continuum model

Next, we derive analytical estimates for the nonlinear motion superimposed on the finitely deformed hSMM system. To this end, we assume that the width of the superimposed motion is much larger than the length scale of the unit cell (i.e., the long-wavelength assumption), and that the superimposed rotation $\theta_w^{[ij]} \ll 1$. By taking the continuum limit of the equations of motion Eq. (22) and retaining the nonlinear terms up to the third order, the continuum governing equations for the superimposed motion can be obtained as,

$$\begin{aligned} M_s \ddot{u}_x &= a_{st}^2 (k_t \partial_{xx} u_x + k_s \partial_{yy} u_x) + \frac{k_t a a_{st}}{\cos \theta_0} \left(\sin \theta_0 + \theta \cos \theta_0 - \theta^2 \frac{\sin \theta_0}{2} \right) \partial_x \theta, \\ M_s \ddot{u}_y &= a_{st}^2 (k_t \partial_{yy} u_y + k_s \partial_{xx} u_y) + \frac{k_t a a_{st}}{\cos \theta_0} \left(\sin \theta_0 + \theta \cos \theta_0 - \theta^2 \frac{\sin \theta_0}{2} \right) \partial_y \theta, \\ J \ddot{\theta} &= \frac{a_{st}^2}{4} \left(k_s a^2 \frac{\cos^2 \theta_0}{\cos^2 \theta_0} - k_t a^2 \frac{\sin^2 \theta_0}{\cos^2 \theta_0} - 4k_\theta \right) (\partial_x \theta + \partial_y \theta) \\ &\quad - \frac{1}{2} k_t a a_{st} \left(2\theta \frac{\cos \theta_0}{\cos \theta_0} + (2 - \theta^2) \frac{\sin \theta_0}{\cos \theta_0} \right) (\partial_x u_x + \partial_y u_y) \\ &\quad + \left(-2k_t a a_{st} \frac{\cos \theta_0}{\cos \theta_0} + 2k_t a^2 \frac{\cos(2\theta_0)}{\cos^2 \theta_0} - 8k_\theta + \frac{MBV_m}{\sqrt{2}} (\sin \theta_0 + \cos \theta_0) \right) \theta \\ &\quad + \left(k_t a a_{st} \frac{\sin \theta_0}{\cos \theta_0} - 2k_t a^2 \frac{\sin(2\theta_0)}{\cos^2 \theta_0} + \frac{MBV_m}{2\sqrt{2}} (\cos \theta_0 - \sin \theta_0) \right) \theta^2 \\ &\quad + \left(k_t a a_{st} \frac{\cos \theta_0}{3\cos \theta_0} - 4k_t a^2 \frac{\cos(2\theta_0)}{3\cos^2 \theta_0} - \frac{MBV_m}{6\sqrt{2}} (\cos \theta_0 + \sin \theta_0) \right) \theta^3, \end{aligned} \quad (23)$$

where $\theta_0 = \theta_0 + \theta_{st}$, and $a_{st} = a(1 + \epsilon_{st}^x) = a(1 + \epsilon_{st}^y)$ is the center-to-center distance of the deformed hSMM. Note that, here, we assume $\epsilon_{st}^x = \epsilon_{st}^y$ (this is in line with the results illustrated in Figs. 3 and 4). For a given magnetic field level B , ϵ_{st}^x , ϵ_{st}^y , and θ_{st} are determined according to Eq. (18). In addition, $u_x(x, y, t)$, $u_y(x, y, t)$, and $\theta(x, y, t)$ are three continuous functions that interpolate the discrete variables $u_{x-w}^{[ij]}$, $u_{y-w}^{[ij]}$, and $\theta_w^{[ij]}$, respectively. Details of the continuum model are given in

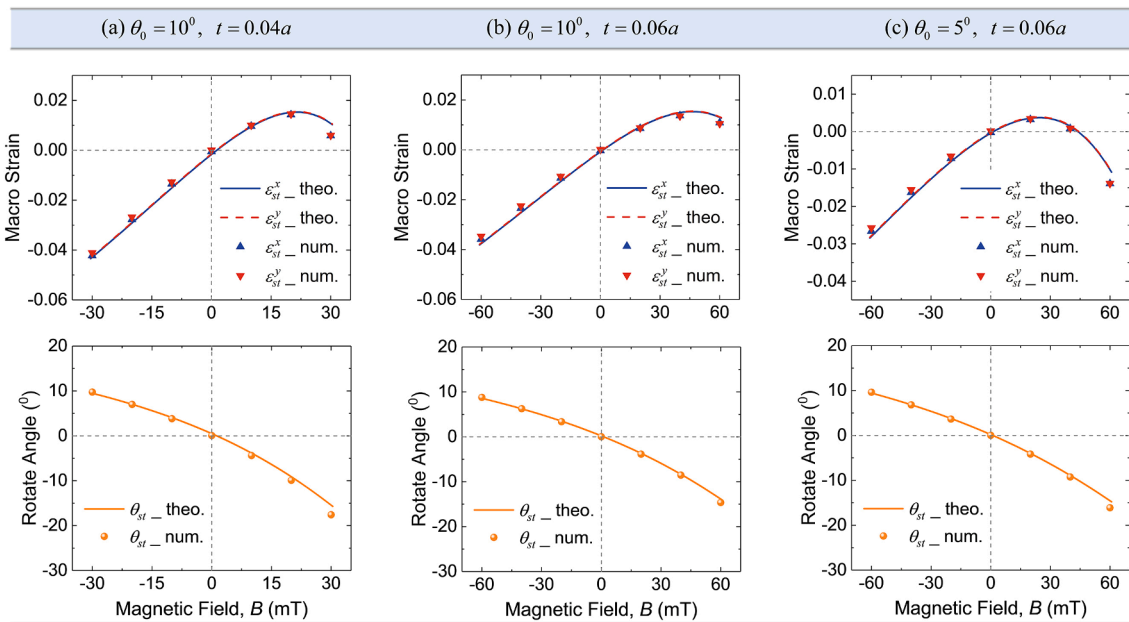


Fig. 4. Magnetic field-induced deformation in hSMM systems with the geometric parameters (a) $\theta_0 = 10^\circ$, and $t = 0.04a$; (b) $\theta_0 = 10^\circ$, and $t = 0.06a$; and (c) $\theta_0 = 5^\circ$, and $t = 0.06a$, with the center-to-center distance fixed at $a = 10$ mm.

Appendix D.

To solve Eq. (23), we consider planar waves propagating in the system and introduce the traveling coordinate $\zeta = x\cos\varphi + y\sin\varphi - ct$, with φ being the angle between the direction of propagation and the x -axis (see Fig. S2 in Appendix D), and c being the pulse velocity. By rewriting Eq. (23) as an expression for ζ , and then integrating Eq. (23)₁ and Eq. (23)₂ with respect to ζ , and substituting them into Eq. (23)₃, we obtain,

$$\partial_{\zeta\zeta}\theta = C_1\theta + C_2\theta^2 + C_3\theta^3, \quad (24)$$

where

$$\begin{aligned} C_1 &= \left(-a^2 \frac{\sin^2\theta_0}{\cos^2\theta_0} (E_x + E_y) - 2a^2 \frac{\cos(2\theta_0)}{\cos^2\theta_0} + 2aa_{st} \frac{\cos\theta_0}{\cos\theta_0} + \frac{8k_0}{k_l} \right. \\ &\quad \left. - \frac{\sqrt{2}MBV_m}{2k_l} (\cos\theta_0 + \sin\theta_0) \right) / F, \\ C_2 &= \left(-3a^2 \frac{\sin(2\theta_0)}{4\cos^2\theta_0} (E_x + E_y) + 2a^2 \frac{\sin(2\theta_0)}{\cos^2\theta_0} - aa_{st} \frac{\sin\theta_0}{\cos\theta_0} \right. \\ &\quad \left. - \frac{\sqrt{2}MBV_m}{4k_l} (\cos\theta_0 - \sin\theta_0) \right) / F, \\ C_3 &= \left(a^2 \frac{1 - 7\cos(2\theta_0)}{12\cos^2\theta_0} (E_x + E_y) + 4a^2 \frac{\cos(2\theta_0)}{3\cos^2\theta_0} - aa_{st} \frac{\cos\theta_0}{3\cos\theta_0} \right. \\ &\quad \left. + \frac{\sqrt{2}MBV_m}{12k_l} (\cos\theta_0 + \sin\theta_0) \right) / F, \end{aligned} \quad (25)$$

with

$$\begin{aligned} E_x &= \frac{\cos^2\varphi}{\cos^2\varphi + \frac{k_s}{k_l}\sin^2\varphi - \frac{M_s c^2}{k_l a_{st}^2}}, \\ E_y &= \frac{\sin^2\varphi}{\sin^2\varphi + \frac{k_s}{k_l}\cos^2\varphi - \frac{M_s c^2}{k_l a_{st}^2}}, \\ F &= -\frac{Jc^2}{k_l} - a^2 a_{st}^2 \frac{\sin^2\theta_0}{4\cos^2\theta_0} + a^2 a_{st}^2 \frac{k_s}{k_l} \frac{\cos^2\theta_0}{4\cos^2\theta_0} - a_{st}^2 \frac{k_0}{k_l}. \end{aligned} \quad (26)$$

4.3. Solitary wave solutions

Eq. (24) is the Klein–Gordon equation with quadratic and cubic nonlinearities (Polyanin and Zaitsev, 2011), admitting well-known solitary wave solutions of the form

$$\theta = \frac{1}{D_1 \pm D_2 \cosh(\zeta/W)}. \quad (27)$$

Eq. (27) defines a solitary wave with characteristic width W and amplitude A_0 ,

$$A_0 = \theta(\zeta = 0) = \frac{1}{D_1 \pm D_2}. \quad (28)$$

Substituting Eq. (27) into Eq. (24) yields,

$$D_1 = -\frac{C_2}{3C_1}, D_2 = \sqrt{\frac{C_2^2}{9C_1^2} - \frac{C_3}{2C_1}}, W = \frac{1}{\sqrt{C_1}}. \quad (29)$$

The existence of the solutions for the solitary waves given by Eq. (27) requires the following:

(i) W is real, namely,

$$C_1 > 0; \quad (30)$$

(ii) D_2 is real, namely,

$$\frac{C_2^2}{9C_1^2} - \frac{C_3}{2C_1} > 0; \text{ and} \quad (31)$$

(iii) the denominator in Eq. (27) is non-zero, namely,

$$D_1 \pm D_2 \cosh(\zeta/W) \neq 0. \quad (32)$$

Deng et al. (2018b) have shown that the violation of Eqs. (30)–(32) may result in the formation of amplitude gaps for the solitary waves. Since $D_2 > 0$ and $\cosh(\zeta/W) \in [1, +\infty)$, Eq. (32) is satisfied only if $|D_1| < D_2$; otherwise, only one of the two solitary solutions defined by Eq. (27) exists. Therefore, there are the following three cases.

- Case 1: $-D_2 < D_1 < D_2$.

Two solitary solutions exist,

$$\theta_+ = \frac{1}{D_1 + D_2 \cosh(\zeta/W)}, \theta_- = \frac{1}{D_1 - D_2 \cosh(\zeta/W)}. \quad (33)$$

- Case 2: $D_1 < -D_2$.

Only one solitary solution exists,

$$\theta_- = \frac{1}{D_1 - D_2 \cosh(\zeta/W)}. \quad (34)$$

- Case 3: $D_1 > D_2$.

Only one solitary solution exists,

$$\theta_+ = \frac{1}{D_1 + D_2 \cosh(\zeta/W)}. \quad (35)$$

4.4. Magnetic field-based tunability of solitary waves

For given geometric parameters, the governing coefficients D_1 , D_2 , and W are functions of the pulse velocity c and the externally applied magnetic field level B . Therefore, the characteristic width and type of solitary waves can be controlled by a magnetic field. Fig. 5a shows the solitary solutions as a function of the applied magnetic field level B . The results are given for hSMM with a center-to-center distance $a = 10$ nm, initial offset angle $\theta_0 = 5^\circ$, and ligament thickness $t = 0.04a$. There are four possible scenarios. i) $-D_2 < D_1 < D_2$ (blue region in Fig. 5a). In this case, there are two solitary solutions defined by θ_+ and θ_- (Eq. (33)), respectively. ii) $D_1 < -D_2$ (the orange domains in Fig. 5a). In this case, there is a single solitary solution defined by θ_- (Eq. (34)). iii) $D_1 > D_2$ (the green regions in Fig. 5a). In this case, there is a single solitary solution defined by θ_+ (Eq. (35)). iv) Any condition from Eqs. (30)–(32) is violated; thus, no solitary solution exists (the gray area in Fig. 5a).

Fig. 5b displays the dependence of the normalized characteristic width W/a of the solitary pulse on the velocity c and the magnetic field level B . Note that the accuracy of the continuum approximation (Eqs. (49) and (50) in Appendix D) reduces significantly as the pulse width becomes comparable to the length scale of the unit cell. Thus, analytically predicted solitons with a relatively small width may not be supported by the discrete system (Deng et al., 2018a). A comparison of Fig. 5a and 5b shows that the solitary pulse width in almost the entire variable domains corresponding to $D_1 < -D_2$ (the orange area in Fig. 5a) and $D_1 > D_2$ (the green area in Fig. 5a) is relatively very small, as indicated by the contour line (the pink curves; here $W/a = 2$ as an example). Therefore, we focus on solitary solutions in the case of $-D_2 < D_1 < D_2$; the system supports two solitary solutions defined by θ_+ and θ_- (Eq. (33)). The amplitudes of rotation corresponding to these two solutions are,

$$A_{\theta_+} = \frac{1}{D_1 + D_2}, A_{\theta_-} = \frac{1}{D_1 - D_2}. \quad (36)$$

Fig. 6 shows the evolution of the rotational amplitudes of the solitary solutions (for the case $-D_2 < D_1 < D_2$) as a function of the pulse

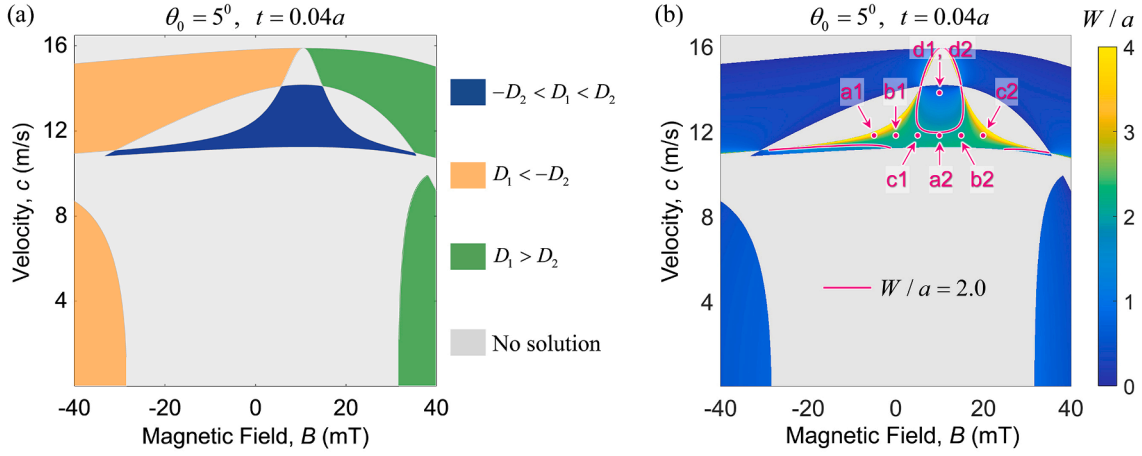


Fig. 5. (a) Effect of the externally applied magnetic field level B on the pulse velocity c and the types of solitary waves supported by a hSMM with geometric parameters $a = 10$ mm, $\theta_0 = 5^\circ$, and $t = 0.04a$. (b) Evolution of the characteristic width W as a function of c and B . The circular markers in (b) indicate the points considered in our numerical analysis, with the results presented in Fig. 9 (points a1–d1) and Fig. 10 (points a2–d2).

velocity c and the magnetic field level B . The results are given for hSMMs with a center-to-center distance $a = 10$ mm, initial offset angle $\theta_0 = 5^\circ$, and ligament thickness $t = 0.04a$ (these parameters are the same as those in Fig. 5). One can see that one solitary solution is characterized by a positive rotational component ($A_{\theta_+} > 0$; see Fig. 6a) and the other by a negative rotational component ($A_{\theta_-} < 0$; see Fig. 6b). This means that in one case, the $[i, j]$ -th square unit rotates clockwise while in the other, it rotates counterclockwise (in both cases, neighboring units rotate in opposite directions). Moreover, the pulse amplitudes of the solitons propagating in our hSMM system can be tuned by the external magnetic field. Specifically, as the magnetic field level B (considering its sign) is increased, the absolute value of A_{θ_+} increases (see Fig. 6a) while the absolute value of A_{θ_-} decreases (see Fig. 6b). Note that the rotational amplitude of the solitons is limited due to two factors. First, contacts between neighboring squares may occur as the rotational angle of the propagating soliton increases. Second, the continuum approximation (Eq. (52)) used to derive our analytical solution requires $|\theta| \ll 1$. Therefore, we consider $0 < A_{\theta_+} < +0.3$ and $-0.3 < A_{\theta_-} < 0$; the contours for $A_{\theta_+} = +0.3$ and $A_{\theta_-} = -0.3$ are shown by the pink curves in Fig. 6a and 6b, respectively.

Finally, we provide the results of the numerical solutions of the ordinary differential equations (ODEs) given by Eqs. (45)–(47), and compare the results with predictions by the continuum approximation. To determine the boundary conditions for the ODEs, the solutions for displacements u_x and u_y are obtained by integrating Eq. (54) in Appendix D,

$$\begin{aligned}
 u_x^\pm &= \frac{aWE_x}{12a_{st}\cos\varphi\cos\theta_0(-D_1^2 + D_2^2)^{5/2}} \left[\pm \theta_\pm^2 \sin\theta_0 \sinh\left(\frac{\zeta}{W}\right) D_2(-D_1^2 + D_2^2)^{3/2} \right. \\
 &\quad \left. + 2H \left(\arctan\left(\frac{D_1 \mp D_2}{\sqrt{-D_1^2 + D_2^2}}\right) - \arctan\left(\frac{D_1 \mp D_2}{\sqrt{-D_1^2 + D_2^2}} \tanh\left(\frac{\zeta}{2W}\right)\right) \right) \right. \\
 &\quad \left. - 3 \left(1 \mp \theta_\pm D_2 \sinh\left(\frac{\zeta}{W}\right) \right) (-\sin\theta_0 D_1 + 2\cos\theta_0(D_1^2 - D_2^2)) \sqrt{-D_1^2 + D_2^2} \right], \\
 u_y^\pm &= \frac{aWE_y}{12a_{st}\sin\varphi\cos\theta_0(-D_1^2 + D_2^2)^{5/2}} \left[\pm \theta_\pm^2 \sin\theta_0 \sinh\left(\frac{\zeta}{W}\right) D_2(-D_1^2 + D_2^2)^{3/2} \right. \\
 &\quad \left. + 2H \left(\arctan\left(\frac{D_1 \mp D_2}{\sqrt{-D_1^2 + D_2^2}}\right) - \arctan\left(\frac{D_1 \mp D_2}{\sqrt{-D_1^2 + D_2^2}} \tanh\left(\frac{\zeta}{2W}\right)\right) \right) \right. \\
 &\quad \left. - 3 \left(1 \mp \theta_\pm D_2 \sinh\left(\frac{\zeta}{W}\right) \right) (-\sin\theta_0 D_1 + 2\cos\theta_0(D_1^2 - D_2^2)) \sqrt{-D_1^2 + D_2^2} \right],
 \end{aligned} \quad (37)$$

where θ_+ and θ_- are given in Eq. (33), and,

$$\begin{aligned}
 H &= 6\cos\theta_0 D_1 (-D_1^2 + D_2^2) + \sin\theta_0 [2D_1^2(1 + 12D_2^2) + D_2^2(1 - 12D_2^2) \\
 &\quad - 12D_1^4].
 \end{aligned} \quad (38)$$

In the numerical analysis, we consider a model comprising 60×120 square units, as illustrated in Fig. 7b. The theoretical solution predicted by Eqs. (33) and (37) is applied as excitation to the units on the left boundary (see Fig. 7a), while the other boundaries are free. We focus on planar solitary waves propagating in the x -direction (i.e., $\varphi = 0$). As such, the component of displacement u_y given in Eq. (37)₂ is zero. Note that the system supports two solitary solutions; thus, the excitation is a combination of θ_+ , u_x^+ , and u_y^+ , or θ_- , u_x^- , and u_y^- . Moreover, to eliminate the effect of boundary mismatch, the 15 layers of units closest to the upper and lower boundaries serve as a perfect matching layer (PML). Damping is added to the equations of motion (the ODEs given by Eqs. (45)–(47) in Appendix C) of units located in the PML, with the distribution of the damping factor given in Fig. 7c.

Fig. 8 shows the numerical results for magnetic field level $B = 0$ mT and pulse velocity $c = 11.8$ m/s (corresponding to point b1 highlighted in Fig. 5b and 6a). The rotational profiles at $T = 15, 30$, and 45 are shown in Fig. 8a (the upper panel), and the displacement profiles in the x - and y -directions at these times are shown in Fig. 8b and c, respectively. The normalized time is defined as $T = ct/a - 30$, with the constant shift representing the position of the solitary pulse on the excitation profile (see Fig. 7a). The evolutions of the rotational component ($\theta_{w}^{[ij]}$ in Fig. 8a) and the component of displacement in the x -direction ($u_{x-w}^{[ij]}/a$ in Fig. 8b) indicate the propagation of an elastic vector soliton – the rotational and translational components of motion are coupled and propagate together without dispersion. Meanwhile, the component of displacement in the y -direction ($u_{y-w}^{[ij]}/a$ in Fig. 8c) is almost zero in the entire discrete model except at units near the upper and lower boundaries. This is because the soliton is excited to propagate along the x -direction (see Fig. 7a). Moreover, we show the spatial-temporal evolution of each component of motion by focusing on the center line (the white line in Fig. 7b) of the considered model, see the lower panel of each subplot. The pulse velocity extracted from the spatial-temporal evolution is 11.6 m/s, very close to the theoretically expected value of 11.8 m/s.

In Fig. 9, we compare the analytical (curves, given by Eqs. (33) and (37)) and the numerical (markers) results. In the numerical simulations, a combination of θ_+ , u_x^+ , and u_y^+ (corresponding to the solitary wave solution characterized by the positive rotational component) is applied

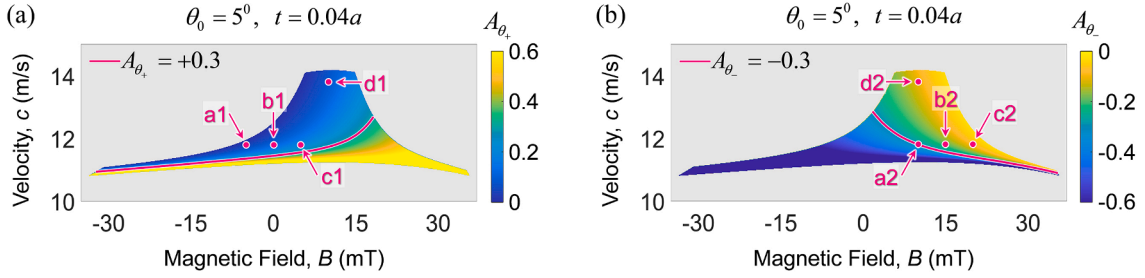


Fig. 6. Evolution of the rotational amplitudes (a) A_{θ_+} and (b) A_{θ_-} as a function of the pulse velocity c and the magnetic field level B . The results are given for a hSMM with the geometric parameters $a = 10$ mm, $\theta_0 = 5^\circ$, and $t = 0.04a$. The circular markers in (a) and (b) denote the points considered in our numerical analysis, with the results presented in Fig. 9 (points a1–d1) and Fig. 10 (points a2–d2), respectively.

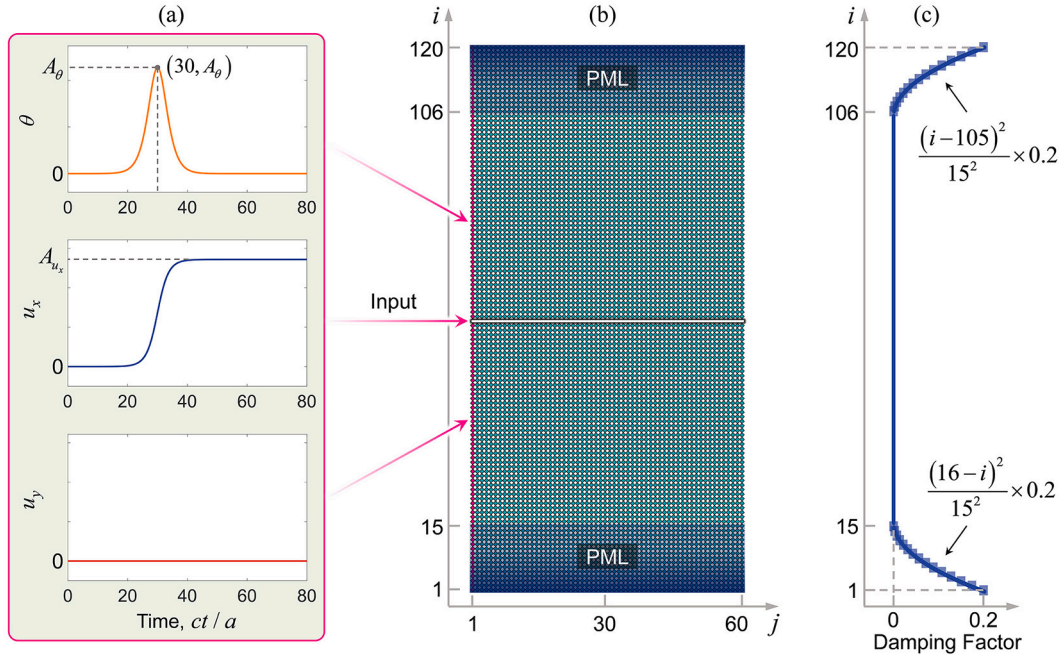


Fig. 7. Numerical analysis of solitary waves propagating in the proposed hSMM system. (a) The theoretical solution given by Eqs. (33) and (37) is applied to the square units on the left boundary of the numerical model. (b) The considered numerical model consists of 60×120 square units. The 15 layers of units closest to the upper and lower boundaries serve as a perfect matching layer (PML) to eliminate the effect of boundary mismatch. The damping factor illustrated in (c) is added to the equations of motion of units in the PML.

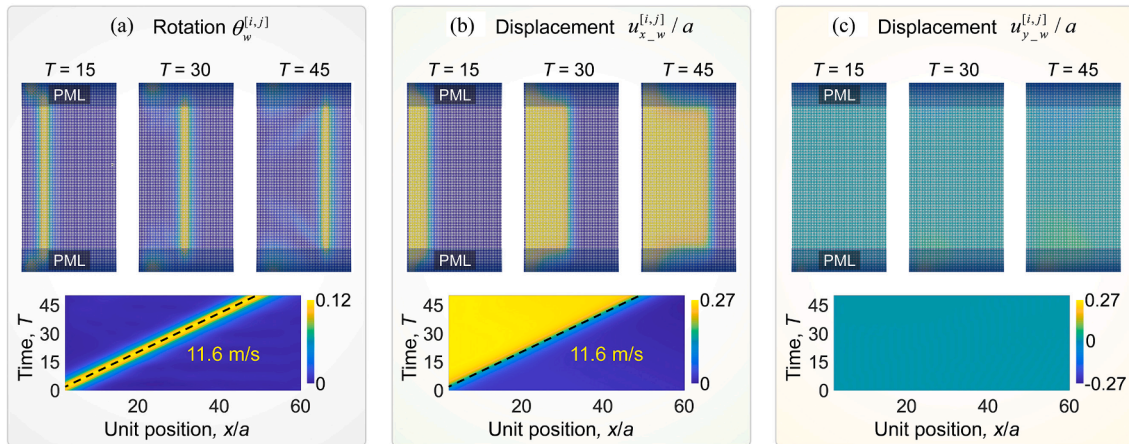


Fig. 8. Numerical solutions for solitary waves propagating in the hSMM system comprising 60×120 square units. The results are given for magnetic field level $B = 0$ mT and pulse velocity $c = 11.8$ m/s (as marked by point b1 in Fig. 5b and 6a). (a) The rotational component. (b) The component of normalized displacement in the x -direction. (c) The component of normalized displacement in the y -direction. In each sub-plot, the upper panel shows the contour plots at $T = 15, 30$, and 45 , while the lower panel presents the spatial-temporal evolution on the center line (the white line in Fig. 7b) of the model.

to the left boundary of the considered mode. The numerical results are obtained by extracting the rotation ($\theta_w^{[i,j]}$) and displacement ($u_{x,w}^{[i,j]}$) along the center line (see the white line in Fig. 7b) of the model. Fig. 9a-d show the rotation (up) and normalized displacement (bottom) profiles for $B = -5$ mT and $c = 11.8$ m/s, $B = 0$ mT and $c = 11.8$ m/s, $B = 5$ mT and $c = 11.8$ m/s, and $B = 10$ mT and $c = 13.8$ m/s, respectively. The characteristic pulse width W and rotational amplitude A_{θ_+} predicted by the continuum model for these cases are highlighted by points a1–d1 in Fig. 5b and 6a, respectively. An excellent agreement is observed between the numerical results and the predictions of our continuum model (see Fig. 9a–c). Both the amplitudes of the rotational and translational components of motion become larger as the externally applied magnetic field level increases from $B = -5$ mT to $B = 5$ mT. However, the system does not support solitons with a sufficiently small width W because the continuum approximation (Eqs. (49) and (50) in Appendix D) used to derive the analytical solution is no longer valid. For example, the excited wave is dispersed during propagation for $B = 10$ mT and $c = 13.8$ m/s (see Fig. 9d; the normalized pulse width, in this case, is $W/a = 0.856$).

For the solitary wave solution characterized by a negative rotational component, a comparison between the analytically and numerically predicted solitary motion profiles is shown in Fig. 10. The excitation in the numerical simulation is a combination of θ_- , u_x^- , and u_y^- . Fig. 10a–d show the rotation (up) and normalized displacement (bottom) profiles for $B = 10$ mT and $c = 11.8$ m/s, $B = 15$ mT and $c = 11.8$ m/s, $B = 20$ mT and $c = 11.8$ m/s, and $B = 10$ mT and $c = 13.8$ m/s, respectively. The characteristic pulse width W and rotational amplitude A_{θ_-} predicted by the continuum model for these cases are highlighted by points a2–d2 in Fig. 5b and 6b. Once again, the numerical results are consistent with the continuum analysis for the solutions to solitary waves with a relatively large pulse width (see, for example, Fig. 10a–c). The amplitudes (both the rotational and translational components) of the solitary pulse decrease as the magnetic field level is increased from $B = 10$ mT to $B = 20$ mT. By contrast, solitary waves are not supported by the system if the pulse width W is small enough (see Fig. 10d, with $W/a = 0.856$).

Our theoretical analysis and computational framework are beneficial for further experiment verification of solitary waves in the proposed hSMM system. In experiments, impact stimulation can be applied to initiate simultaneous rotation and displacement of the units positioned at the excitation boundary of a finite hSMM lattice. The applied impact signal is characterized by the impulse displacement and impulse velocity, which can be determined by the unit's maximum displacement and maximum velocity, respectively. Taking the hSMM system in Fig. 7 as an

example, the impulse displacement of the impact signal will be $u^{\max} = \max(u_x)$, where u_x is given in Eq. (37). Meanwhile, the impulse velocity of the impact signal will be $v^{\max} = \max(-c \cdot \partial_z u_x)$, with c being the pulse velocity of the predicted solitary solution. In addition, we note that in this study, we did not consider material damping effects that may originate from the soft PDMS matrix due to its viscoelasticity. In experiments, it is plausible that the displacement amplitude of soliton will decrease along propagation due to the material damping. To realize solitary wave propagation in experiments, the following approaches may be utilized. i) One can focus on waves propagating for a finite (relatively short) distance, such as before reflection at the boundary of the tested sample. ii) One may consider solitary solutions with relatively large pulse amplitude A_{θ} and small pulse width W . In this case, the nonlinear response of the system is strongly activated, and solitary waves are expected to form within a relatively short propagation distance (Deng et al., 2017). Experimentally, the solitary pulse will be subjected to a weak decrease in displacement amplitude due to the short propagation distance.

5. Conclusions

In this study, we have investigated the behavior of hSMMs consisting of an array of square units (with magnetic inclusion) connected at their vertices via thin and deformable ligaments. We analyzed the hSMM subjected to a magnetic field along one of the principal material directions. First, we derived the macroscopic strains (along the two principal directions) and rotation of the hSMMs with remanent magnetizations under activation by external magnetic fields. The derivation is built on an equivalent discrete model comprising rigid square units connected at their vertices by springs. The analytical estimates agree well with the finite element simulations. The analytical and numerical results indicate that the deformation mode (shrinking or expansion) and the rotating direction of units of the proposed hSMM system can be controlled by changing the level and direction of the applied magnetic field.

Second, we examined the propagation of vector solitary waves in the hSMMs undergoing finite strains in the presence of an external magnetic field. We derived the governing equations for the superimposed nonlinear motion by building on the discrete mass-spring model. We obtained the continuum governing equations for the superimposed motion in the continuum limit. The continuum model predicted the characteristic pulse width and amplitude of solitary waves supported by

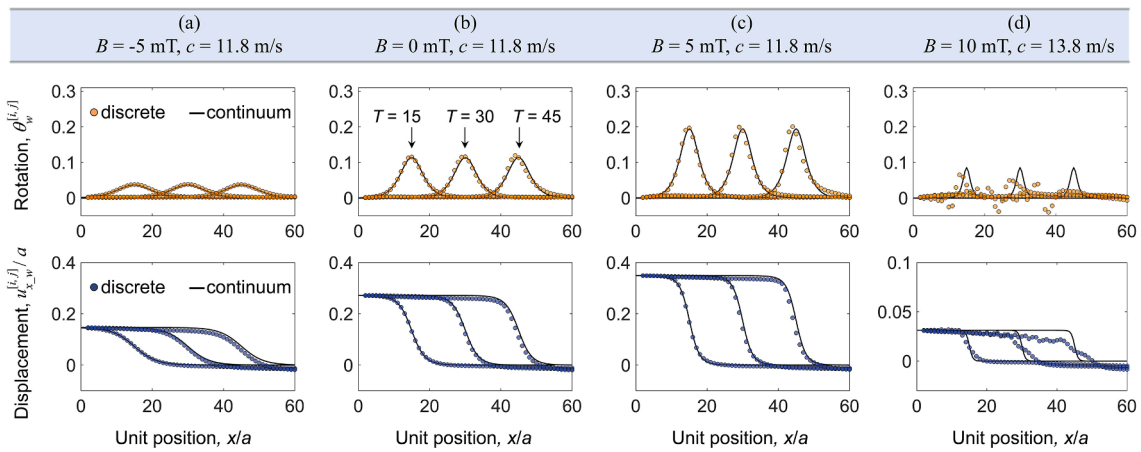


Fig. 9. Numerical (markers) and analytical (curves) results of solitary waves in a hSMM with geometric parameters $a = 10$ mm, $\theta_0 = 5^\circ$, and $t = 0.04a$. Profiles of rotation (up) and normalized displacement in the x -direction (bottom) for: (a) $B = -5$ mT and $c = 11.8$ m/s, (b) $B = 0$ mT and $c = 11.8$ m/s, (c) $B = 5$ mT and $c = 11.8$ m/s, and (d) $B = 10$ mT and $c = 13.8$ m/s (as marked by points a1–d1 in Fig. 5b and 6a). The profiles at $T = 15, 30$, and 45 are presented in each subplot.

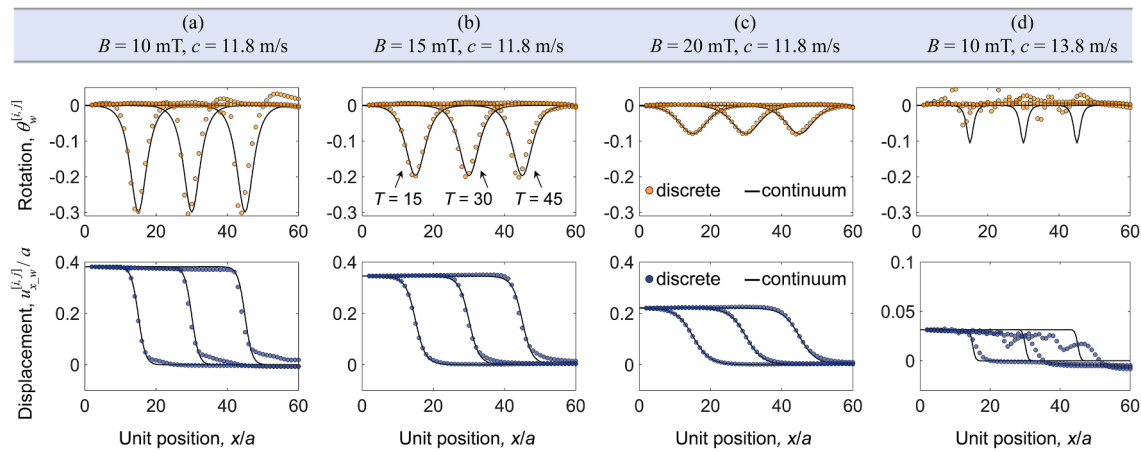


Fig. 10. Numerical (markers) and analytical (curves) results of solitary waves in a hSMM with geometric parameters $a = 10$ mm, $\theta_0 = 5^\circ$, and $t = 0.04a$. Profiles of rotation (up) and normalized displacement in the x -direction (bottom) for: (a) $B = 10$ mT and $c = 11.8$ m/s, (b) $B = 15$ mT and $c = 11.8$ m/s, (c) $B = 20$ mT and $c = 11.8$ m/s, and (d) $B = 10$ mT and $c = 13.8$ m/s (as marked by points a2–d2 in Fig. 5b and 6b). The profiles at $T = 15, 30$, and 45 are presented in each subplot.

the proposed hSMM system. The continuum model was further validated by the numerical solution of the corresponding ODEs for the discrete mass-spring model. Thanks to the magneto-mechanical coupling, the pulse width and amplitude of solitons propagating in the proposed hSMM, and even their *on* or *off* states, could be tuned by a remotely applied magnetic field. These findings suggest that the proposed magnetoactive metamaterial can be applied as an untethered solitary wave switch. Moreover, the results provided in this paper can guide the design of novel materials and structures with unusual and enhanced wave tunability and nonlinear elastic properties.

Declaration of Competing Interest

The authors declare that they have no known competing financial interests or personal relationships that could have appeared to influence the work reported in this paper.

Data availability

Data will be made available on request.

Acknowledgements

QZ thanks the support of the National Natural Science Foundation of China through Grant No. 12002030. SR thanks for the support of the European Research Council (ERC) through Grant No. 852281- MAGIC.

Appendices A–D. Supplementary data

Supplementary data to this article can be found online at <https://doi.org/10.1016/j.ijsolstr.2023.112396>.

References

- Bilal, O.R., Foehr, A., Daraio, C., 2017a. Bistable metamaterial for switching and cascading elastic vibrations. *PNAS* 114 (18), 4603–4606.
- Bilal, O.R., Foehr, A., Daraio, C., 2017b. Reprogrammable Phononic Metasurfaces. *Adv. Mater.* 29 (39), 1700628.
- Chen, V.W., Arora, N., Goshkoderia, A., Willey, C.L., Turgut, Z., Buskohl, P.R., Rudykh, S., Juhl, A.T., 2023. Mechanical instability tuning of a magnetorheological elastomer composite laminate. *Compos. B Eng.* 251, 110472.
- Chen, Y., Liu, X., Hu, G., 2019. Topological phase transition in mechanical honeycomb lattice. *J. Mech. Phys. Solids* 122, 54–68.
- Chen, Y., Li, X., Hu, G., Haberman, M.R., Huang, G., 2020. An active mechanical Willis meta-layer with asymmetric polarizabilities. *Nat. Commun.* 11, 3681.
- Chen, H., Nassar, H., Huang, G.L., 2018. A study of topological effects in 1D and 2D mechanical lattices. *J. Mech. Phys. Solids* 117, 22–36.
- Chen, T., Pauly, M., Reis, P.M., 2021a. A reprogrammable mechanical metamaterial with stable memory. *Nature* 589 (7842), 386–390.
- Chen, B.-g., Upadhyaya, N., Vitelli, V., 2014. Nonlinear conduction via solitons in a topological mechanical insulator. *PNAS* 111 (36), 13004–13009.
- Chen, Y., Zhang, Q., Zhang, Y., Xia, B., Liu, X., Zhou, X., Chen, C., Hu, G., 2021b. Research progress of elastic topological materials. *Adv. Mech.* 51, 189–256.
- Chong, C., Porter, M.A., Kevrekidis, P.G., Daraio, C., 2017. Nonlinear coherent structures in granular crystals. *J. Phys. Condens. Matter* 29 (41), 413003.
- Christodoulides, D.N., Lederer, F., Silberberg, Y., 2003. Discretizing light behaviour in linear and nonlinear waveguide lattices. *Nature* 424 (6950), 817–823.
- Ciambella, J., Favata, A., Tomassetti, G., 2018. A nonlinear theory for fibre-reinforced magneto-elastic rods. *Proceed. Roy. Soc. A: Mathemat., Phys. Eng. Sci.* 474 (2209), 20170703.
- Coulais, C., Soulas, D., Alù, A., 2017. Static non-reciprocity in mechanical metamaterials. *Nature* 542 (7642), 461–464.
- Cui, J., Huang, T.-Y., Luo, Z., Testa, P., Gu, H., Chen, X.-Z., Nelson, B.J., Heyderman, L.J., 2019. Nanomagnetic encoding of shape-morphing micromachines. *Nature* 575 (7781), 164–168.
- da Costa, B., Linn, L., Danas, K., Bodelot, L., 2022. Towards 4D Printing of Very Soft Heterogeneous Magnetoactive Layers for Morphing Surface Applications via Liquid Additive Manufacturing. *Polymers (Basel)* 14, 1684.
- Deng, B., Raney, J.R., Tournat, V., Bertoldi, K., 2017. Elastic Vector Solitons in Soft Architected Materials. *Phys. Rev. Lett.* 118, 204102.
- Deng, B., Tournat, V., Bertoldi, K., 2018a. Effect of predeformation on the propagation of vector solitons in flexible mechanical metamaterials. *Phys. Rev. E* 98, 053001.
- Deng, B., Wang, P., He, Q., Tournat, V., Bertoldi, K., 2018b. Metamaterials with amplitude gaps for elastic solitons. *Nat. Commun.* 9, 3410.
- Deng, B., Mo, C., Tournat, V., Bertoldi, K., Raney, J.R., 2019a. Focusing and Mode Separation of Elastic Vector Solitons in a 2D Soft Mechanical Metamaterial. *Phys. Rev. Lett.* 123, 024101.
- Deng, B., Zhang, Y., He, Q., Tournat, V., Wang, P., Bertoldi, K., 2019b. Propagation of elastic solitons in chains of pre-deformed beams. *New J. Phys.* 21 (7), 073008.
- Deng, B., Chen, L., Wei, D., Tournat, V., Bertoldi, K., 2020. Pulse-driven robot: Motion via solitary waves. *Sci. Adv.* 6, eaaz1166.
- Deng, B., Raney, J.R., Bertoldi, K., Tournat, V., 2021. Nonlinear waves in flexible mechanical metamaterials. *J. Appl. Phys.* 130 (4), 040901.
- Destrade, M., Ogden, R.W., 2011. On magneto-acoustic waves in finitely deformed elastic solids. *Math. Mech. Solids* 16 (6), 594–604.
- Erb, R.M., Libanori, R., Rothfuchs, N., Studart, A.R., 2012. Composites reinforced in three dimensions by using low magnetic fields. *Science* 335 (6065), 199–204.
- Foehr, A., Bilal, O.R., Huber, S.D., Daraio, C., 2018. Spiral-Based Phononic Plates: From Wave Beaming to Topological Insulators. *Phys. Rev. Lett.* 120, 205501.
- Galich, P.I., Rudykh, S., 2017. Shear Wave Propagation and Band Gaps in Finitely Deformed Dielectric Elastomer Laminates: Long Wave Estimates and Exact Solution. *J. Appl. Mech.* 84, 091002.
- Garcia-Gonzalez, D., Ter-Yesayants, T., Moreno-Mateos, M.A., Lopez-Donaire, M.L., 2023. Hard-magnetic phenomena enable autonomous self-healing elastomers. *Compos. B Eng.* 248, 110357.
- Goshkoderia, A., Chen, V., Li, J., Juhl, A., Buskohl, P., Rudykh, S., 2020. Instability-induced pattern formations in soft magnetoactive composites. *Phys. Rev. Lett.* 124, 158002.
- Goshkoderia, A., Rudykh, S., 2017. Stability of magnetoactive composites with periodic microstructures undergoing finite strains in the presence of a magnetic field. *Compos. B Eng.* 128, 19–29.
- Hu, W., Lum, G.Z., Mastrangeli, M., Sitti, M., 2018. Small-scale soft-bodied robot with multimodal locomotion. *Nature* 554 (7690), 81–85.

- Hussein, M.I., Leamy, M.J., Ruzzene, M., 2014. Dynamics of Phononic Materials and Structures: Historical Origins, Recent Progress, and Future Outlook. *Appl. Mech. Rev.* 66, 040802.
- Hwang, M., Arrieta, A.F., 2021. Extreme Frequency Conversion from Soliton Resonant Interactions. *Phys. Rev. Lett.* 126, 073902.
- Itskov, M., Khiêm, V.N., 2016. A polyconvex anisotropic free energy function for electro- and magneto-rheological elastomers. *Math. Mech. Solids* 21 (9), 1126–1137.
- Jin, L., Khajepourian, R., Mueller, J., Rafsanjani, A., Tournat, V., Bertoldi, K., Kochmann, D.M., 2020. Guided transition waves in multistable mechanical metamaterials. *PNAS* 117 (5), 2319–2325.
- Karami Mohammadi, N., Galich, P.I., Krushynska, A.O., Rudykh, S., 2019. Soft magnetoactive laminates: large deformations, transverse elastic waves and band gaps tunability by a magnetic field. *J. Appl. Mech.* 86, 111001.
- Keip, M.-A., Rambausk, M., 2016. A multiscale approach to the computational characterization of magnetorheological elastomers. *Int. J. Numer. Meth. Eng.* 107 (4), 338–360.
- Kim, Y., Yuk, H., Zhao, R., Chester, S.A., Zhao, X., 2018. Printing ferromagnetic domains for unethered fast-transforming soft materials. *Nature* 558 (7709), 274–279.
- Krushynska, A.O., Torrent, D., Aragón, A.M., Ardito, R., Bilal, O.R., Bonello, B., Bosia, F., Chen, Y., Christensen, J., Colombi, A., Cummer, S.A., Djafari-Rouhani, B., Fraternali, F., Galich, P.I., Garcia, P.D., Groby, J.-P., Guenneau, S., Haberman, M.R., Hussein, M.I., Janbaz, S., Jiménez, N., Khelif, A., Laude, V., Mirzaali, M.J., Packo, P., Palermo, A., Pennec, Y., Picó, R., López, M.R., Rudykh, S., Serra-Garcia, M., Sotomayor Torres, C.M., Starkey, T.A., Tournat, V., Wright, O.B., 2023. Emerging topics in nanophononics and elastic, acoustic, and mechanical metamaterials: an overview. *Nanophotonics* 12, 659–686.
- Liang, X., Fu, H., Crosby, A.J., 2022. Phase-transforming metamaterial with magnetic interactions. *PNAS* 119 (1).
- Liu, X.N., Hu, G.K., Huang, G.L., Sun, C.T., 2011. An elastic metamaterial with simultaneously negative mass density and bulk modulus. *Appl. Phys. Lett.* 98 (25), 251907.
- Liu, H., Zhang, Q., Zhang, K., Hu, G., Duan, H., 2019. Designing 3D Digital Metamaterial for Elastic Waves: From Elastic Wave Polarizer to Vibration Control. *Adv. Sci.* 6 (16), 1900401.
- Lucarini, S., Hossain, M., Garcia-Gonzalez, D., 2022. Recent advances in hard-magnetic soft composites: Synthesis, characterisation, computational modelling, and applications. *Compos. Struct.* 279, 114800.
- Marin-Palomo, P., Kemal, J.N., Karpov, M., Kordts, A., Pfeifle, J., Pfeiffer, M.H.P., Trocha, P., Wolf, S., Brasch, V., Anderson, M.H., Rosenberger, R., Vijayan, K., Freude, W., Kippenberg, T.J., Koos, C., 2017. Microresonator-based solitons for massively parallel coherent optical communications. *Nature* 546 (7657), 274–279.
- Maugin, G.A., 1981. Wave motion in magnetizable deformable solids. *Int. J. Eng. Sci.* 19 (3), 321–388.
- Memoli, G., Calep, M., Asakawa, M., Sahoo, D.R., Drinkwater, B.W., Subramanian, S., 2017. Metamaterial bricks and quantization of meta-surfaces. *Nat. Commun.* 8, 14608.
- Mokhtari, A.A., Lu, Y., Srivastava, A., 2019. On the emergence of negative effective density and modulus in 2-phase phononic crystals. *J. Mech. Phys. Solids* 126, 256–271.
- Mooney, M., 1951. The viscosity of a concentrated suspension of spherical particles. *J. Colloid Sci.* 6 (2), 162–170.
- Moreno-Mateos, M.A., Hossain, M., Steinmann, P., Garcia-Gonzalez, D., 2022. Hybrid magnetorheological elastomers enable versatile soft actuators. *npj Comput. Mater.* 8, 162.
- Nadkarni, N., Arrieta, A.F., Chong, C., Kochmann, D.M., Daraio, C., 2016. Unidirectional Transition Waves in Bistable Lattices. *Phys. Rev. Lett.* 116, 244501.
- Nassar, H., Chen, Y.Y., Huang, G.L., 2019. Isotropic polar solids for conformal transformation elasticity and cloaking. *J. Mech. Phys. Solids* 129, 229–243.
- Nassar, H., Chen, Y.Y., Huang, G.L., 2020. Polar metamaterials: A new outlook on resonance for cloaking applications. *Phys. Rev. Lett.* 124, 084301.
- Ortigueira, R., Gil, A.J., 2016. A new framework for large strain electromechanics based on convex multi-variable strain energies: Conservation laws, hyperbolicity and extension to electro-magneto-mechanics. *Comput. Methods Appl. Mech. Eng.* 309, 202–242.
- Palagi, S., Mark, A.G., Reigh, S.Y., Melde, K., Qiu, T., Zeng, H., Parmeggiani, C., Martella, D., Sanchez-Castillo, A., Kapernaum, N., 2016. Structured light enables biomimetic swimming and versatile locomotion of photoresponsive soft microrobots. *Nat. Mater.* 15, 647–653.
- Pathak, P., Arora, N., Rudykh, S., 2022. Magnetoelastic instabilities in soft laminates with ferromagnetic hyperelastic phases. *Int. J. Mech. Sci.* 213, 106862.
- Polyanin, A., Zaitsev, V., 2011. Handbook of nonlinear partial differential equations. Chapman and Hall/CRC, New York.
- Porter, M.A., Kevrekidis, P.G., Daraio, C., 2015. Granular crystals: Nonlinear dynamics meets materials engineering. *Phys. Today* 68 (11), 44–50.
- Raney, J.R., Nadkarni, N., Daraio, C., Kochmann, D.M., Lewis, J.A., Bertoldi, K., 2016. Stable propagation of mechanical signals in soft media using stored elastic energy. *PNAS* 113 (35), 9722–9727.
- Rudykh, S., Bertoldi, K., 2013. Stability of anisotropic magnetorheological elastomers in finite deformations: A micromechanical approach. *J. Mech. Phys. Solids* 61 (4), 949–967.
- Russell, J.S., 1844. Report on waves. Report of the fourteenth meeting of the British Association for the Advancement of Science, 311–390.
- Sen, S., Hong, J., Bang, J., Avalos, E., Doney, R., 2008. Solitary waves in the granular chain. *Phys. Rep.* 462 (2), 21–66.
- Singhal, T., Kim, E., Kim, T.-Y., Yang, J., 2017. Weak bond detection in composites using highly nonlinear solitary waves. *Smart Mater. Struct.* 26, 055011.
- Slesarenko, V., 2020. Planar Mechanical Metamaterials with Embedded Permanent Magnets. *Materials* 13, 1313.
- Srivastava, A., 2016. Metamaterial properties of periodic laminates. *J. Mech. Phys. Solids* 96, 252–263.
- Tang, S.-Y., Zhang, X., Sun, S., Yuan, D., Zhao, Q., Yan, S., Deng, L., Yun, G., Zhang, J., Zhang, S., Li, W., 2018. Versatile microfluidic platforms enabled by novel magnetorheological elastomer microactuators. *Adv. Funct. Mater.* 28, 1705484.
- Tian, T.F., Li, W.H., Deng, Y.M., 2011. Sensing capabilities of graphite based MR elastomers. *Smart Mater. Struct.* 20, 025022.
- Wang, P., Casadei, F., Shan, S., Weaver, J.C., Bertoldi, K., 2014. Harnessing buckling to design tunable locally resonant acoustic metamaterials. *Phys. Rev. Lett.* 113, 014301.
- Wang, L., Zheng, D., Harker, P., Patel, A.B., Guo, C.F., Zhao, X., 2021. Evolutionary design of magnetic soft continuum robots. *Proceedings of the National Academy of Sciences of the United States of America* 118, e2021922118.
- Wang, P., Lu, L., Bertoldi, K., 2015. Topological Phononic Crystals with One-Way Elastic Edge Waves. *Phys. Rev. Lett.* 115, 104302.
- Wang, Z., Zhang, Q., Zhang, K., Hu, G., 2016. Tunable Digital Metamaterial for Broadband Vibration Isolation at Low Frequency. *Adv. Mater.* 28, 9857–9861.
- Wu, B., Su, Y., Chen, W., Zhang, C., 2017. On guided circumferential waves in soft electroactive tubes under radially inhomogeneous biasing fields. *J. Mech. Phys. Solids* 99, 116–145.
- Yan, D., Abbasi, A., Reis, P.M., 2021. A comprehensive framework for hard-magnetic beams: Reduced-order theory, 3D simulations, and experiments. *Int. J. Solids Struct.* 257, 111319.
- Yasuda, H., Miyazawa, Y., Charalampidis, E.G., Chong, C., Kevrekidis, P.G., Yang, J., 2019. Origami-based impact mitigation via rarefaction solitary wave creation. *Science. Advances* 5, eaau2835.
- Yasuda, H., Korpas, L.M., Raney, J.R., 2020. Transition Waves and Formation of Domain Walls in Multistable Mechanical Metamaterials. *Phys. Rev. Appl.* 13, 054067.
- Yu, K., Fang, N.X., Huang, G., Wang, Q., 2018. Magnetoactive Acoustic Metamaterials. *Adv. Mater.* 30, 1706348.
- Zareei, A., Deng, B., Bertoldi, K., 2020. Harnessing transition waves to realize deployable structures. *Proceedings of the National Academy of Sciences of the United States of America* 117, 4015–4020.
- Zhang, Q., Rudykh, S., 2022. Magneto-deformation and transverse elastic waves in hard-magnetic soft laminates. *Mech. Mater.* 169, 104325.
- Zhang, Q., Yan, D., Zhang, K., Hu, G., 2015. Pattern transformation of heat-shrinkable polymer by three-dimensional (3D) printing technique. *Sci. Rep.* 5, 8936.
- Zhang, Q., Zhang, K., Hu, G., 2016. Smart three-dimensional lightweight structure triggered from a thin composite sheet via 3D printing technique. *Sci. Rep.* 6, 22431.
- Zhang, Q., Chen, Y., Zhang, K., Hu, G., 2019a. Programmable elastic valley Hall insulator with tunable interface propagation routes. *Extreme Mech. Lett.* 28, 76–80.
- Zhang, H.K., Chen, Y., Liu, X.N., Hu, G.K., 2020a. An asymmetric elastic metamaterial model for elastic wave cloaking. *J. Mech. Phys. Solids* 135, 103796.
- Zhang, Q., Chen, Y., Zhang, K., Hu, G., 2020b. Dirac degeneracy and elastic topological valley modes induced by local resonant states. *Phys. Rev. B* 101, 014101.
- Zhang, Q., Guo, D., Hu, G., 2021. Tailored Mechanical Metamaterials with Programmable Quasi-Zero-Stiffness Features for Full-Band Vibration Isolation. *Adv. Funct. Mater.* 31, 2101428.
- Zhang, Q., Cherkasov, A.V., Arora, N., Hu, G., Rudykh, S., 2023. Magnetic field-induced asymmetric mechanical metamaterials. *Extreme Mech. Lett.* 59, 101957.
- Zhang, Y., Li, B., Zheng, Q.S., Genin, G.M., Chen, C.Q., 2019b. Programmable and robust static topological solitons in mechanical metamaterials. *Nat. Commun.* 10, 5605.
- Zhao, R., Kim, Y., Chester, S.A., Sharma, P., Zhao, X., 2019. Mechanics of hard-magnetic soft materials. *J. Mech. Phys. Solids* 124, 244–263.
- Zhu, R., Liu, X.N., Hu, G.K., Sun, C.T., Huang, G.L., 2014. Negative refraction of elastic waves at the deep-subwavelength scale in a single-phase metamaterial. *Nat. Commun.* 5, 5510.